Supplement of The Cryosphere, 20, 1523–1542, 2026
https://doi.org/10.5194/tc-20-1523-2026-supplement

The Cryosphere Open Access EGU

Supplement of

Sea ice albedo bounded data assimilation and its impact on modeling: a regional approach

Joseph F. Rotondo et al.

Correspondence to: Joseph F. Rotondo (jrotondo@uw.edu)

S1 Adaptive Inflation for Sea Ice DA in QCEFF

The introduction of a bounded DA scheme complicates the use of classical inflation techniques. In traditional ensemble DA, multiplicative inflation is often applied to artificially increase model spread, enhancing the ensemble's ability to capture observed variability (Anderson and Anderson, 1999). However, this approach becomes problematic when applied to bounded variables, which must remain within strict physical limits. For example, during the melt season, SIC within a grid cell can approach zero. When μ is near zero, inflating the spread by a factor intended for Gaussian distributions can produce ensemble members that fall below zero–an unphysical state–or expand the distribution in a way that still fails to include nearby observed values. If, after inflation, the observation still falls outside the ensemble's acceptable range (here defined as within $\pm 2\sigma$ of the mean), the DA framework may reject it as inconsistent with the model prior. This mismatch highlights the challenge of using symmetric inflation schemes for variables with hard physical bounds and skewed distributions near those bounds.

Observation rejections can also occur even when values are not near physical bounds. These rejections stem from insufficient ensemble spread rather than model limitations, especially during rapid changes when μ diverges from the true model-generated observation. This issue is especially common during the melt season, when fast transitions often associated with albedo feedback and driven by melt-ponding, refreezing, or snowfall introduce variability that bounded ensemble systems struggle to accommodate.

To address these challenges, we apply a temporally varying adaptive inflation scheme available in DART, which enforces a minimum model spread (Gharamti, 2018). This scheme models inflation factors as inverse-gamma distributed random variables. Inflation values evolve over time alongside the ensemble state, with their means and variances updated based on observational input. In our implementation within the QCEFF (Quantile Conserving Ensemble Filter Framework), the adaptive inflation diverges from its original formulation. Rather than enforcing strict bounds through priors or hard constraints–as in traditional bounded inflation schemes–the QCEFF-compatible version emphasizes physical consistency and conservation across the ensemble. This reformulation decouples inflation from rigid statistical boundaries and instead aligns it with the QCEFF's diagnostic balance principles (Anderson, 2022, 2023).

This adaptive inflation framework ensures stability and consistency by preserving the integrity of the initial ensemble spread introduced during the spin-up phase. We fix the minimum inflation factor at 1.0, maintaining the original ensemble spread prior to data assimilation. The upper bound is set at 50.0, although this limit is rarely approached due to the physical constraints imposed by the bounded DA scheme. To regulate how inflation evolves over time, we constrain the standard deviation of the inverse gamma distribution used to sample the inflation factor. Specifically, the distribution's standard deviation must be no smaller than 0.6, ensuring a minimum level of ensemble variability, and the distribution's width is restricted such that the inflation standard deviation cannot grow or shrink by more than a factor of 1.05 per time step. These constraints, informed by prior work (e.g., Wieringa et al., 2024), are designed to prevent overly abrupt changes in inflation while allowing sufficient flexibility to respond to dynamic error growth.

S2 Sensitivity to Observational Noise Realizations

While generating synthetic observations, we applied random perturbations drawn from a specified distribution around the TRUTH state. This is standard practice in perfect-model assimilation experiments to simulate measurement uncertainty. In our case, observations were generated using the `perfect_model_obs` tool in DART, which employed the QCEFF with bounded, non-Gaussian likelihoods. These were configured through the `obs_error_info` table by prescribing physical bounds for each variable. As a result, the synthetic observations were sampled from piecewise-linear distributions consistent with the bounded likelihoods, rather than simple Gaussians.

Because this approach represents a relatively novel method for generating synthetic observations—particularly in sea ice data assimilation–we assessed whether variability in specific realizations of random noise could influence assimilation performance. We repeated a subset of six SIAL-only assimilation experiments under the medium uncertainty configuration, each using a distinct random seed to produce three separate realizations of observational noise (with identical error magnitude and statistical bounds). Root Mean Square Error (RMSE) was computed for SIC and SIT across all regions and ensemble truth members.

As shown in Figure S1, differences in RMSE across noise realizations were negligible, and the relative ordering of assimilation performance among experiments remained unchanged. This result is consistent with theoretical expectations: because all realizations are drawn from the same bounded likelihood defined in `obs_error_info`, and the same table is used during both observation generation and assimilation, the system remains statistically consistent. Moreover, the ensemble nature of the assimilation—using 30 members—and the high spatial and temporal observation density act to dampen the influence of any individual realization. Over many assimilation cycles, random fluctuations are averaged out, and the filter converges on similar solutions regardless of the specific noise pattern.

We further note that some minor variation could emerge during early cycles, when fewer observations have been assimilated and their influence is more localized. However, in long-term (many month) perfect-model experiments such as this one, where the system is well-observed and observations are generated in a self-consistent manner, the stochasticity of synthetic noise has limited impact. These findings reinforce the robustness of DART's QCEFF system for assimilating bounded, non-Gaussian observational errors in high-density sea ice observing systems.

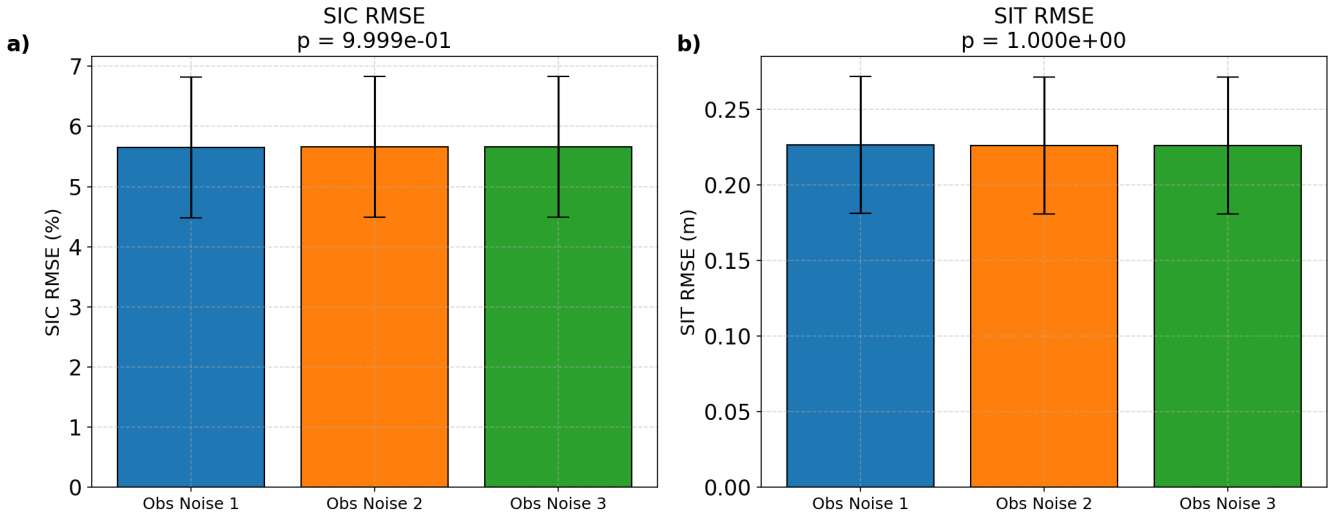

Figure S1. Impact of random observational noise on SIAL assimilation (medium uncertainty case) for SIC (a) and SIT (b) RMSEs, averaged across six ensemble truth members and all regions. Each of the three "Obs Noise" levels corresponds to a different random realization of observational noise with the same magnitude (2σ error). Error bars show 95% confidence intervals based on ensemble–region combinations. SIC cutoffs from Fig. S2 were utilized when calculating SIT RMSE. A one-way ANOVA was performed to test whether RMSE values significantly differ between noise realizations. The resulting p-values near 1.0 indicate no statistically significant difference across noise realizations, suggesting that the DA system effectively accounts for uncertainty generated from random noise. This result supports the robustness of DART's QCEFF to random perturbations when the observation error variance is correctly specified. The use of 30 ensemble members in the assimilation step likely contributes to this robustness, as the effects of random noise are averaged out across the ensemble.

S3 SIAL P-Values for Comparison

Table S1: Statistical significance of SIAL RMSE comparisons ($p < 0.05$), based on Fig. 5. Comparisons not involving SIAL (e.g., SIT vs. Free Run) are excluded. Regions not shown indicate cases where no SIAL assimilation configurations were statistically distinguishable from other assimilation types.

Region	Comparison	p-value	Better Performer
SIC RMSE – SIAL Comparisons			
Barents	SIAL (Low Error) vs SIAL (Medium Error)	0.0010	SIAL (Low Error)
	SIAL (Low Error) vs SIAL (High Error)	0.0010	SIAL (Low Error)
	SIAL (Medium Error) vs SIAL (High Error)	0.0010	SIAL (Medium Error)
	SIAL (Medium Error) vs All Variables	0.0010	All Variables
	SIAL (High Error) vs All Variables	0.0010	All Variables
	SIAL (Low Error) vs SIT	0.0068	SIAL (Low Error)
	SIAL (Low Error) vs Free Run	0.0137	SIAL (Low Error)
	SIAL (Medium Error) vs Free Run	0.0186	SIAL (Medium Error)
	SIC vs SIAL (High Error)	0.0322	SIC

Continued on next page

Table S1 (continued)

Region	Comparison	p-value	Better Performer
	SIAL (Medium Error) vs SIT	0.0322	SIAL (Medium Error)
	SIAL (High Error) vs SIC and SIT	0.0420	SIC and SIT
CoastalCanada	SIC vs SIAL (Medium Error)	0.0010	SIC
	SIC vs SIAL (High Error)	0.0010	SIC
	SIAL (Low Error) vs Free Run	0.0020	SIAL (Low Error)
	SIAL (Medium Error) vs SIC and SIT	0.0020	SIC and SIT
	SIAL (Medium Error) vs All Variables	0.0020	All Variables
	SIAL (Medium Error) vs Free Run	0.0020	SIAL (Medium Error)
	SIAL (High Error) vs SIC and SIT	0.0020	SIC and SIT
	SIAL (High Error) vs All Variables	0.0020	All Variables
	SIAL (High Error) vs Free Run	0.0020	SIAL (High Error)
	SIC vs SIAL (Low Error)	0.0068	SIC
	SIAL (Low Error) vs SIAL (High Error)	0.0137	SIAL (Low Error)
	SIAL (Low Error) vs SIC and SIT	0.0137	SIC and SIT
	SIAL (Low Error) vs All Variables	0.0247	All Variables
	SIAL (Low Error) vs SIAL (Medium Error)	0.0420	SIAL (Low Error)
SibChuk	SIAL (Medium Error) vs SIC and SIT	0.0004	SIC and SIT
	SIAL (Medium Error) vs All Variables	0.0006	All Variables
	SIAL (High Error) vs SIC and SIT	0.0008	SIC and SIT
	SIAL (High Error) vs All Variables	0.0010	All Variables
	SIAL (Low Error) vs SIAL (Medium Error)	0.0010	SIAL (Low Error)
	SIAL (Low Error) vs SIAL (High Error)	0.0010	SIAL (Low Error)
	SIAL (Low Error) vs Free Run	0.0010	SIAL (Low Error)
	SIC vs SIAL (Medium Error)	0.0015	SIC
	SIC vs SIAL (High Error)	0.0021	SIC
	SIAL (Low Error) vs SIT	0.0186	SIAL (Low Error)
	SIAL (High Error) vs SIT	0.0195	SIT
	SIAL (Medium Error) vs SIT	0.0244	SIT
SIT RMSE – SIAL Comparisons			
Barents	SIAL (High Error) vs SIC and SIT	0.0068	SIC and SIT
	SIAL (High Error) vs SIT	0.0098	SIT
	SIAL (Medium Error) vs SIC and SIT	0.0137	SIC and SIT
	SIAL (Medium Error) vs SIT	0.0420	SIT
	SIAL (Medium Error) vs All Variables	0.0420	All Variables
	SIAL (High Error) vs All Variables	0.0420	All Variables
CoastalCanada	SIAL (Medium Error) vs All Variables	0.0001	All Variables
	SIAL (High Error) vs All Variables	0.0001	All Variables
	SIAL (Low Error) vs All Variables	0.0001	All Variables
	SIAL (Medium Error) vs SIC and SIT	0.0005	SIC and SIT
	SIAL (Medium Error) vs SIT	0.0005	SIT
	SIAL (Low Error) vs SIC and SIT	0.0008	SIC and SIT
	SIAL (Low Error) vs SIT	0.0008	SIT
	SIAL (High Error) vs SIT	0.0015	SIT

Continued on next page

Table S2. SIC cutoff percentages by region, based on the first location where the average $m < 0.05$.

Region	SIC Cutoff (%)
Barents Sea	2.1
Beaufort Sea	3.6
Central Arctic	0.0
Coastal Canada	19.5
Siberian-Chukchi Sea	10.9

Table S1 (continued)

Region	Comparison	p-value	Better Performer
	SIAL (High Error) vs SIC and SIT	0.0016	SIC and SIT
	SIAL (Medium Error) vs Free Run	0.0048	Free Run
	SIAL (Low Error) vs Free Run	0.0071	Free Run
	SIAL (High Error) vs Free Run	0.0307	Free Run
SibChuk	SIAL (Medium Error) vs SIT	0.0002	SIT
	SIAL (Medium Error) vs SIC and SIT	0.0007	SIC and SIT
	SIAL (Low Error) vs Free Run	0.0010	Free Run
	SIAL (Medium Error) vs Free Run	0.0010	Free Run
	SIAL (High Error) vs SIT	0.0010	SIT
	SIAL (High Error) vs SIC and SIT	0.0010	SIC and SIT
	SIAL (High Error) vs Free Run	0.0010	Free Run
	SIAL (Low Error) vs All Variables	0.0020	All Variables
	SIAL (Medium Error) vs All Variables	0.0020	All Variables
	SIAL (High Error) vs All Variables	0.0020	All Variables
	SIAL (Low Error) vs SIT	0.0046	SIT
	SIAL (Low Error) vs SIC and SIT	0.0118	SIC and SIT

S4 SIT RMSE Calculation

When calculating $SIT_{agg} = \frac{\sum_{n=1}^{n_{cat}=5} vice_n}{SIC_{agg}}$, a cutoff threshold on SIC is needed to prevent artificially inflated SIT uncertainties. The SIT_{agg} estimate often exhibits non-Gaussian behavior, including a heavy upper tail due to elevated $vice_n$ values despite low SIC_{agg} (Zhang et al., 2018).

To mitigate this issue, we iteratively examined the SIT RMSE distribution for each region under varying SIC cutoff thresholds. For each region, we selected the lowest SIC threshold at which the average RMSE slope across all assimilation experiments dropped below 0.05 ($m < 0.05$), thereby avoiding artificial inflation of SIT error. We acknowledge that the chosen slope for cutoff analysis is arbitrary, but results differed only slightly at lower m-values. The resulting region-specific SIC cutoff values are summarized in Table S2. Corresponding SIT RMSE distribution plots for each threshold are provided in Figure S2.

S5 `Icepack` Parameter Selection

Here we provide the `Icepack` parameter selections used in this study to ensure reproducibility (Table S3). Most parameter choices follow the default `Icepack` values. We conducted a brief sensitivity test (not shown) in which the snow grain radius, r_{snw}, was varied to assess its influence on the correlation between SIC and SIAL, and between SIT and SIAL. Across the range of observable values, we found negligible differences in SIC–SIAL and SIT–SIAL correlations in all regions, except in the Beaufort Sea, where modest but statistically significant changes in correlation were observed.

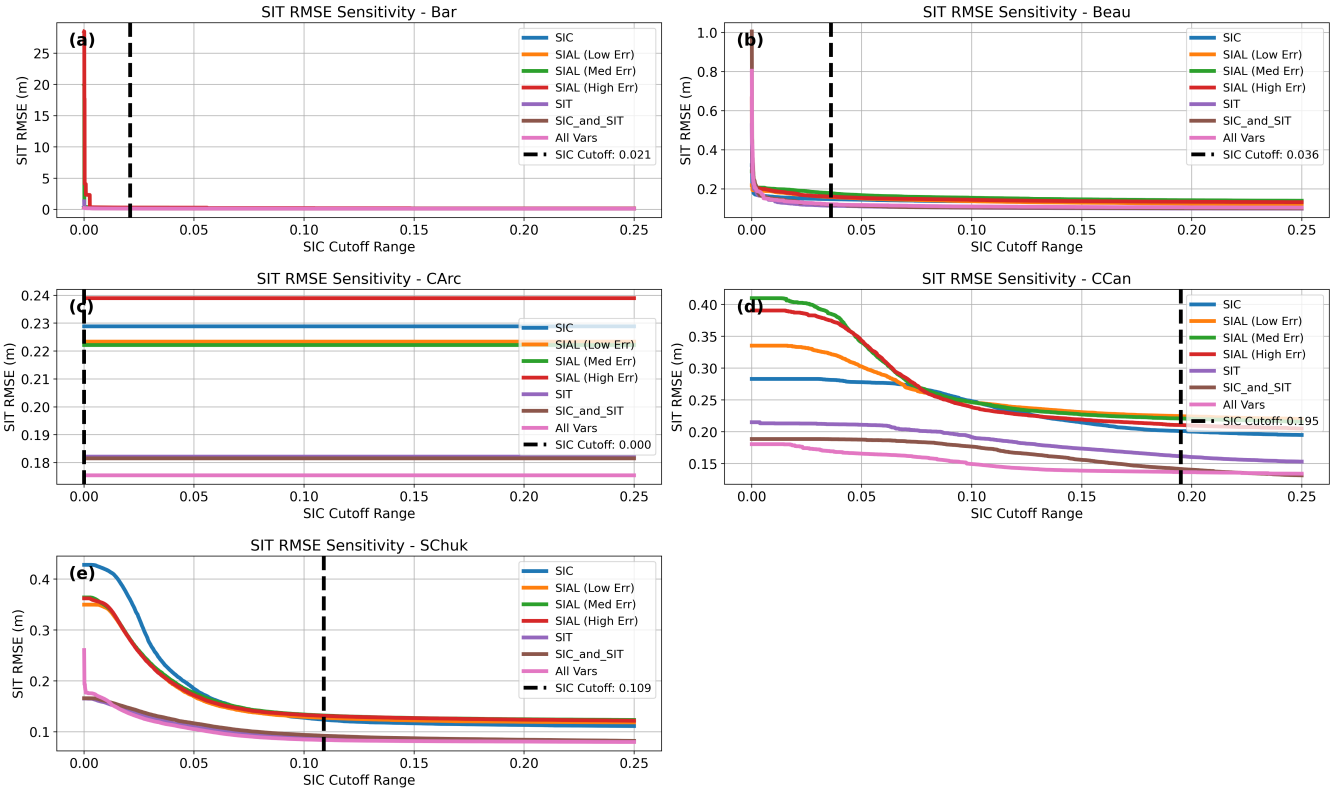

Figure S2. Sensitivity of SIT RMSE to SIC cutoff thresholds across four Arctic regions: Barents Sea (a), Central Arctic (b), Coastal Canada (c), and Siberian-Chukchi Sea (d). Each line represents a different assimilation experiment setup, including SIC-only, SIAL with varying uncertainty levels, SIT-only, and all variables combined. The SIC cutoff is defined as the first SIC threshold at which the average slope (m) of SIT RMSE with respect to increasing SIC cutoff is less than 0.05. Vertical dashed lines indicate these cutoff points, expressed as fractional SIC values: 0.021 (Barents Sea), 0.036 (Beaufort Sea), 0.000 (Central Arctic), 0.195 (Coastal Canada), and 0.109 (Siberian-Chukchi Sea).

Table S3. Sea ice and albedo-related tuning parameters specified in Icepack for the spinup, free run, and assimilation experiments.

Parameter	Icepack Variable Name	Default Value	Units	Description
Snow grain radius	r_snw	1.5	unitless	Snow grain radius tuning parameter
Ice surface scattering layer	hi_ssl	0.05	m	Ice surface scattering layer thickness
Snow surface scattering layer	hs_ssl	0.04	m	Snow surface scattering layer thickness
Snow melt grain radius	rsnw_mlt	1500.0	$kg/m^2/s$	Melting snow grain radius
Melt pond drainage timescale	dt_mlt	1.0	days	Drainage timescale for melt ponds
Snow thermal conductivity	ksno	0.3	W/m/K	Thermal conductivity of snow
Ice density	rhoi	917.0	kg/m^3	Density of sea ice
Snow density	rhos	330.0	kg/m^3	Density of snow
Ridging work parameter	Cf	17	unitless	Ratio of ridging work to potential energy change
Ice–ocean drag coefficient	dragio	0.00536	unitless	Drag coefficient at the ice–ocean interface

S6 Melt Pond Parameterization Selection

During the review of this manuscript we discovered that the melt pond scheme parameterization greatly matters for `Icepack` ice and albedo progression throughout the melt season. Within `Icepack` version 1.4.0, two melt pond parameterizations are available (a third parameterization `sealvl_pnd` is introduced in later versions but is not considered here): a level melt pond scheme and a topographic melt pond scheme (CICE Consortium, 2025). In both approaches, melt ponds are represented within

each ice thickness category by their fractional area, a_{pnd}, and mean depth, h_{pnd}, and form once snow has fully melted and the ice surface reaches the melting point.

In the level melt pond scheme, meltwater accumulates on locally flat ice surfaces. Pond volume evolves according to

$$\frac{dV_{pnd}}{dt} = M_s - D, \tag{1}$$

where M_s is the surface meltwater production and D represents drainage. Pond area increases with stored meltwater up to a prescribed maximum,

$$a_{pnd} = \min\left(a_{pnd,\max}, \frac{V_{pnd}}{h_{pnd,\max}}\right), \tag{2}$$

with pond depth given by $h_{pnd} = V_{pnd}/a_{pnd}$. Drainage is parameterized as a function of ice thickness and permeability, allowing more efficient drainage through thinner ice.

The topographic melt pond scheme accounts for subgrid ice surface relief by distributing meltwater according to a prescribed probability density function of surface height. Pond fraction is determined by the fraction of the ice surface lying below the meltwater fill level,

$$a_{pnd} = \int_{-\infty}^{z_w} p(z)\, dz, \tag{3}$$

where $p(z)$ is the surface height distribution and z_w is the water level set by available meltwater volume. Pond depth follows from the difference between z_w and the mean flooded surface height. This formulation allows pond area to expand rapidly early in the melt season and saturate once topographic depressions are filled.

In both schemes, melt ponds reduce surface albedo through an area-weighted combination of snow, bare ice, and ponded water, enhancing absorbed shortwave radiation. During freeze-up, ponds refreeze and are converted to bare ice, with no memory of pond geometry retained between melt seasons.

S6.1 Limitations of the level melt pond scheme under prescribed deformation

The level melt pond scheme in `Icepack` is generally regarded as robust and physically consistent for a wide range of applications, and has been recommended for many configurations due to its numerical stability and limited reliance on poorly constrained surface topography parameters (E. Hunke, pers. comm.). However, in experiments where ice deformation is prescribed rather than prognostic, this scheme can produce unrealistically extensive ponding under certain conditions.

In this study, ice deformation is imposed using opening and closing rates estimated from the SHEBA field campaign (Uttal et al., 2002), which strongly suppresses the development of subgrid-scale surface roughness associated with ridging and rafting for seasonal ice. As a result, the simulated ice surface remains anomalously flat relative to observations in seasonal locations, particularly in regions where mechanical deformation is known to be an important control on melt pond evolution. Within the level melt pond framework, this lack of surface relief effectively maximizes the available flat area for pond formation, leading to excessive pond coverage during the melt season.

This behavior is most pronounced in the Coastal Canada and Siberian Chukchi Sea regions, where summer ice is frequently deformed by wind-driven convergence and shear (Lei et al., 2021; Plante et al., 2025). In these regions, realistic melt pond evolution depends on topographic constraints that limit pond expansion and promote drainage. When these constraints are absent, the level melt pond scheme systematically overestimates pond fraction, amplifying albedo reductions and enhancing surface melt through positive radiative feedbacks. For this reason, the topographic melt pond scheme was used in these locations as a better representation of true melt pond conditions. Figure S3 further supports this claim–the SIAL of the *ice-covered* portion of the grid cell much better matches observations under the topographic melt pond scheme as opposed to the level melt pond scheme (this significant difference is not observed in the remaining three regions, not shown). We restrict our analysis to the *ice-covered* portions of each grid cell to enable a direct comparison between observations and model behavior in surface type transitions (i.e., snow, bare ice, and melt ponds) during the melt season, while avoiding the influence of inherent SIC biases in `Icepack`.

These results do not indicate a deficiency in the level melt pond parameterization itself, but rather highlight its sensitivity to the representation of ice surface roughness. In configurations with fully prognostic ice dynamics, deformation-generated topography implicitly constrains pond formation. When deformation is externally prescribed and surface relief is underestimated, alternative formulations that explicitly account for subgrid topography may provide a more appropriate representation of melt pond evolution for regional analyses. Thus, the authors suggest carefully reviewing the melt pond parameterization when using standalone `Icepack`.

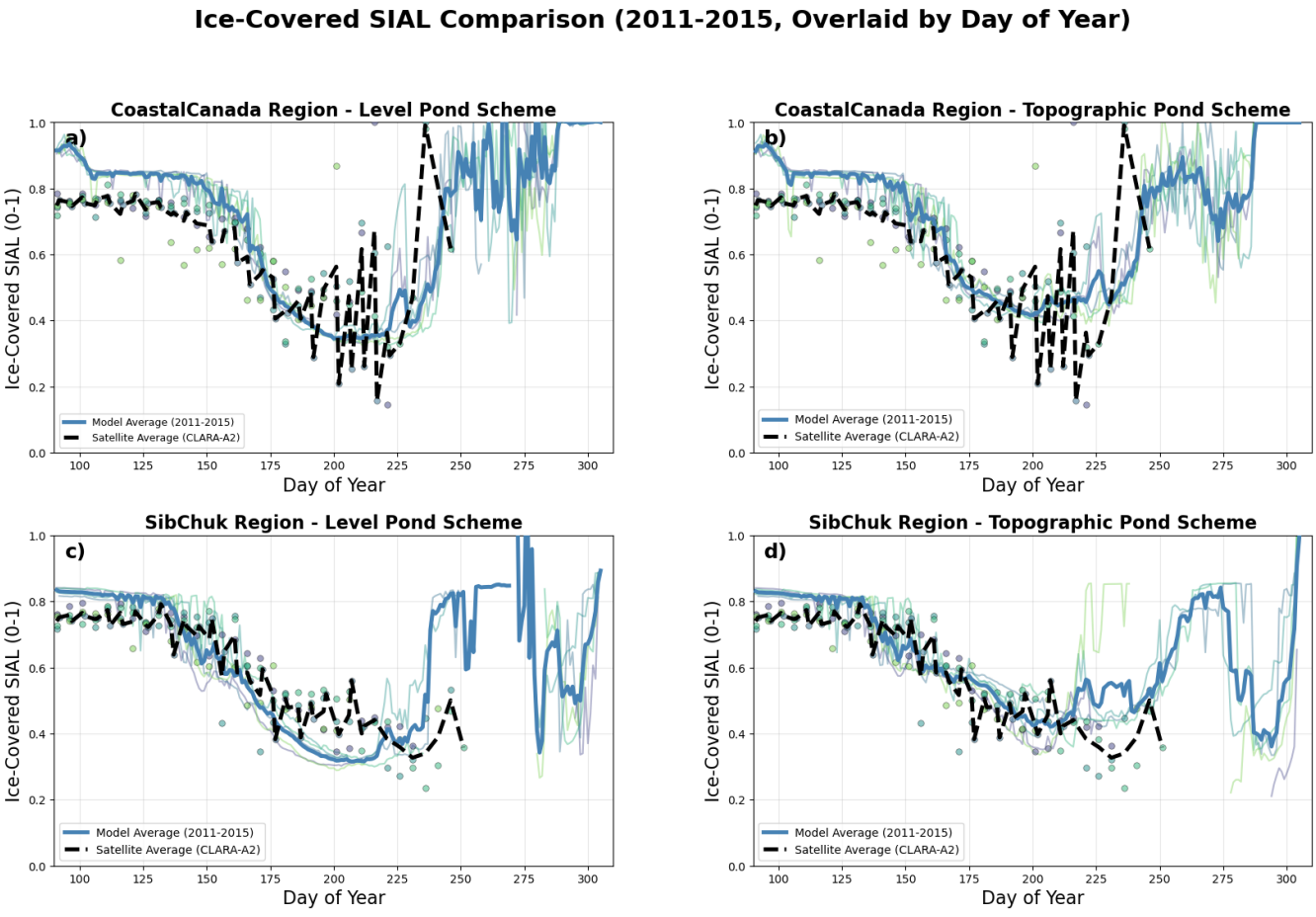

Figure S3. Melt pond parameterization comparison of SIAL over *ice-covered* portions of the grid cell for Coastal Canada (a–b) and the Siberian–Chukchi Sea (c–d), averaged over the melt season (2011–2015). Thin colored lines (blue to yellow) show individual years from the model simulations, while the thick blue line denotes the ensemble mean `Icepack` SIAL. Colored scatter points represent individual satellite observations for each year, and the dashed black line shows the satellite observation average derived from CLARA-A3 SIAL combined with NOAA CDR SIC (Riihelä et al., 2024; Meier et al., 2024). In both regions, the topographic melt pond scheme exhibits significantly improved agreement with observations relative to the level scheme. Comparable performance differences were not observed in other regions; therefore, the level melt pond parameterization was used for all remaining regional analyses.

References

Anderson, J. L.: A Quantile-Conserving Ensemble Filter Framework. Part I: Updating an Observed Variable, Monthly Weather Review, 150, 1061–1074, https://doi.org/10.1175/MWR-D-21-0229.1, publisher: American Meteorological Society Section: Monthly Weather Review, 2022.

Anderson, J. L.: A Quantile-Conserving Ensemble Filter Framework. Part II: Regression of Observation Increments in a Probit and Probability Integral Transformed Space, Monthly Weather Review, 151, 2759–2777, https://doi.org/10.1175/MWR-D-23-0065.1, publisher: American Meteorological Society Section: Monthly Weather Review, 2023.

Anderson, J. L. and Anderson, S. L.: A Monte Carlo Implementation of the Nonlinear Filtering Problem to Produce Ensemble Assimilations and Forecasts, Monthly Weather Review, 127, 2741–2758, https://doi.org/10.1175/1520-0493(1999)127<2741:AMCIOT>2.0.CO;2, publisher: American Meteorological Society Section: Monthly Weather Review, 1999.

CICE Consortium: Icepack Documentation, Los Alamos National Laboratory, https://readthedocs.org/projects/apcraig-icepack/downloads/pdf/latest/, accessed: 2025-05-29, 2025.

Gharamti, M. E.: Enhanced Adaptive Inflation Algorithm for Ensemble Filters, Monthly Weather Review, 146, 623–640, https://doi.org/10.1175/MWR-D-17-0187.1, publisher: American Meteorological Society Section: Monthly Weather Review, 2018.

Lei, R., Hoppmann, M., Cheng, B., Zuo, G., Gui, D., Cai, Q., Belter, H. J., and Yang, W.: Seasonal changes in sea ice kinematics and deformation in the Pacific sector of the Arctic Ocean in 2018/19, The Cryosphere, 15, 1321–1341, https://doi.org/10.5194/tc-15-1321-2021, 2021.

Meier, W., Fetterer, F., Windnagel, A., Stewart, J. S., and Stafford, T.: NOAA/NSIDC Climate Data Record of Passive Microwave Sea Ice Concentration, Version 5, https://doi.org/10.7265/RJZB-PF78, 2024.

Plante, M., Lemieux, J., Tremblay, L. B., Bouchat, A., Ringeisen, D., Blain, P., Howell, S. E. L., Brady, M., Komarov, A. S., Duval, B., Yakuden, L., and Labelle, F.: A sea ice deformation and rotation rate dataset (2017–2023) from the Environment and Climate Change Canada automated sea ice tracking system (ECCC-ASITS), Earth System Science Data, 17, 423–??, https://doi.org/10.5194/essd-17-423-2025, 2025.

Riihelä, A., Jääskeläinen, E., and Kallio-Myers, V.: Four decades of global surface albedo estimates in the third edition of the CM SAF cLoud, Albedo and surface Radiation (CLARA) climate data record, Earth System Science Data, 16, 1007–1028, https://doi.org/10.5194/essd-16-1007-2024, publisher: Copernicus GmbH, 2024.

Uttal, T., Curry, J. A., McPhee, M. G., Perovich, D. K., Moritz, R. E., Maslanik, J. A., Guest, P. S., Stern, H. L., Moore, J. A., Turenne, R., Heiberg, A., Serreze, M. C., Wylie, D. P., Persson, O. G., Paulson, C. A., Halle, C., Morison, J. H., Wheeler, P. A., Makshtas, A., Welch, H., Shupe, M. D., Intrieri, J. M., Stamnes, K., Lindsey, R. W., Pinkel, R., Pegau, W. S., Stanton, T. P., and Grenfell, T. C.: Surface Heat Budget of the Arctic Ocean, Bulletin of the American Meteorological Society, 83, 255–276, https://doi.org/10.1175/1520-0477(2002)083<0255:SHBOTA>2.3.CO;2, 2002.

Wieringa, M. M., Riedel, C., Anderson, J. L., and Bitz, C. M.: Bounded and categorized: targeting data assimilation for sea ice fractional coverage and nonnegative quantities in a single-column multi-category sea ice model, The Cryosphere, 18, 5365–5382, https://doi.org/10.5194/tc-18-5365-2024, publisher: Copernicus GmbH, 2024.

Zhang, Y.-F., Bitz, C. M., Anderson, J. L., Collins, N., Hendricks, J., Hoar, T., Raeder, K., and Massonnet, F.: Insights on Sea Ice Data Assimilation from Perfect Model Observing System Simulation Experiments, Journal of Climate, 31, 5911–5926, https://doi.org/10.1175/JCLI-D-17-0904.1, publisher: American Meteorological Society Section: Journal of Climate, 2018.